ACS Energy LETTERS

http://pubs.acs.org/journal/aelccp

Optimal Interfacial Band Bending Achieved by Fine Energy Level Tuning in Mixed-Halide Perovskite Solar Cells

Matyas Daboczi, Sinclair R. Ratnasingham, Lokeshwari Mohan, Chenfeng Pu, Iain Hamilton, Yi-Chun Chin, Martyn A. McLachlan, and Ji-Seon Kim*

Cite This: ACS Energy Lett. 2021, 6, 3970−3981

Read Online

ACCESS | Metrics & More | Article Recommendations | Supporting Information

ABSTRACT: Most highly efficient perovskite solar cells employ mixed iodide−bromide photoactive layers; however, understanding the beneficial effect of the low (5−15 mol %) bromide content is incomplete. Here, a series of $MAPb(I_{1-x}Br_x)_3$ perovskite layers are investigated to understand the origin of the high peak power conversion efficiency (19.2%) observed at small bromide content ($0.10 \leq x \leq 0.125$). For the $x = 0.125$ perovskite, 200 meV shallower energy levels are revealed, accompanied by a reduced density of trap states and stable tetragonal mixed-halide phase with compressed unit cell. In contrast, the higher bromide content samples ($x > 0.125$) show deeper energy levels, cubic perovskite crystal structure, and signs of halide segregation. Surface photovoltage measurements unveil an undesirable band bending at the hole transport layer/perovskite interface for $MAPbI_3$ and $x > 0.125$ mixed-halide layers, which is eliminated for the $x = 0.125$ perovskite because of its shallower Fermi level, enabling enhanced device performance.

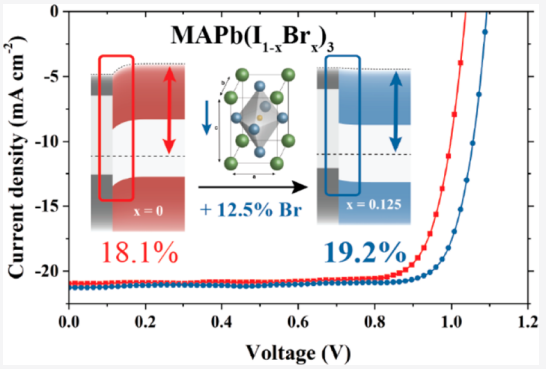

Compositional engineering has played a crucial role in the development of perovskite solar cells. The first methylammonium lead iodide ($MAPbI_3$) based devices with power conversion efficiencies (PCE) of 3−4%[1] have been improved by applying mixed-halide perovskite layers, reaching PCEs above 10%[2−5] and leading the way toward the highest performing mixed-cation, mixed-halide perovskite solar cells currently exceeding 20%[6−10] with certified record PCE of 25.5%.[11]

One of the main aims of applying mixed-halide anions in the perovskite layer is to tune the bandgap of the photoactive material, which is critical to maximize the efficiency of both single-junction and multijunction solar cells.[12−16] Incorporating increasing quantities of bromide into triiodide perovskite absorbers allows an almost linear tuning of the optical bandgap for both methylammonium- and formamidinium-based semiconductor layers between 1.6−2.3 eV and 1.5−2.2 eV, respectively.[17−19] Importantly, rather than just modifying the bandgap, altering the halide composition can also have positive effects on the crystallization process, the resulting morphology, as well as the crystal phase and its stability.[20,21] $MAPbI_3$ is mostly observed in the tetragonal phase at room temperature, and $MAPbBr_3$ is mostly observed in the cubic phase; there is a transition between the two phases around 20 mol % bromide content for the mixed-halide samples.[18,22−25]

An intensively studied phenomenon of mixed iodide−bromide perovskites is the illumination-induced segregation of halide anions, resulting in lower-bandgap iodide-rich (and higher-bandgap bromide-rich) domains, that manifests itself in the red-shift of the main photoluminescence (PL) peak.[26−29] This process can be slowed down or eliminated by applying mixed cations in the perovskite layer;[30−33] however, it has been shown that the main loss mechanism in mixed-halide-based solar cells is related to increased trap densities rather than to halide segregation, leading to significant nonradiative recombination losses.[34] Importantly, reducing the density of trap states was also linked to suppressed halide segregation providing a strategy that could enhance both the PCE and stability of mixed-halide photovoltaic devices.[35,36]

Received: September 21, 2021
Accepted: October 19, 2021
Published: October 21, 2021

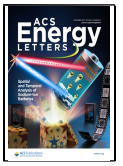

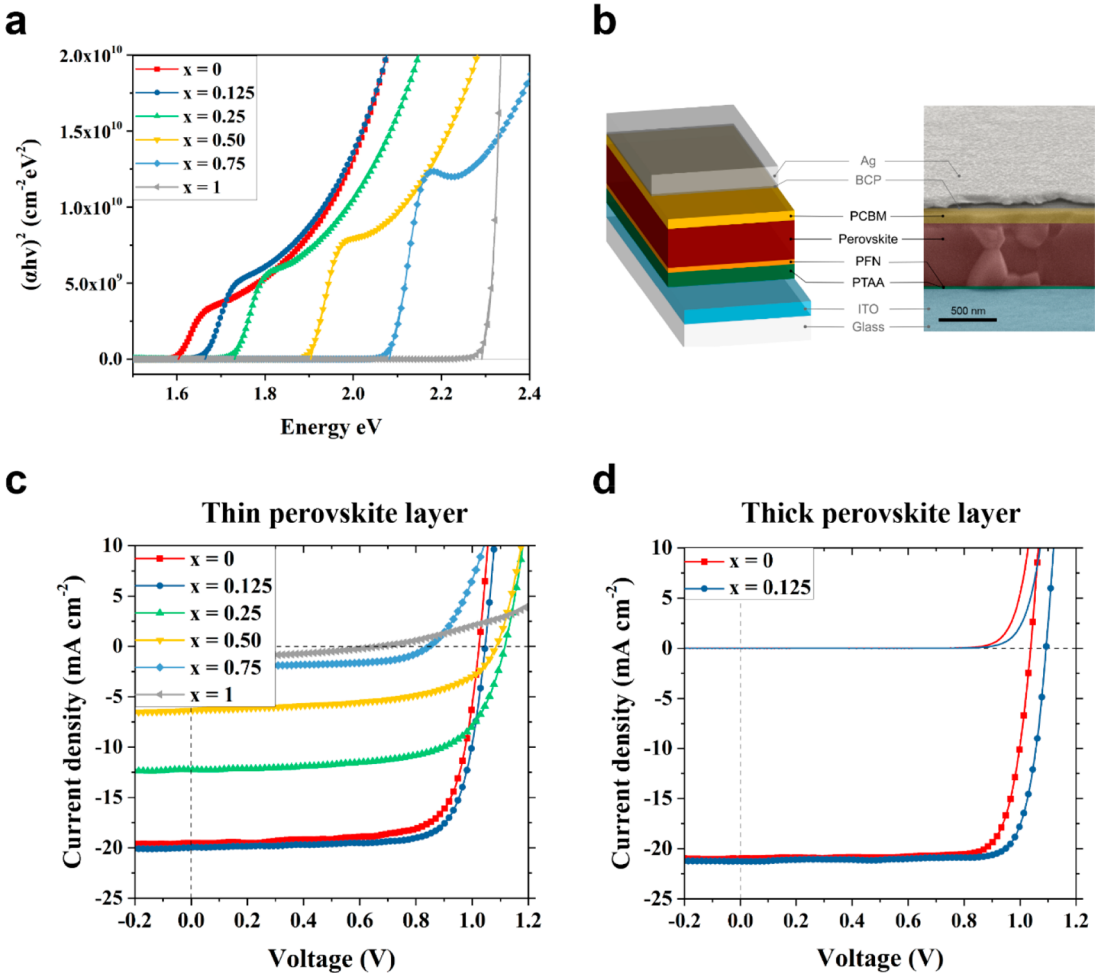

Figure 1. Optical characterization and device performance of $MAPb(I_{1-x}Br_x)_3$ perovskite samples from $x = 0$ ($MAPbI_3$) to $x = 1$ ($MAPbBr_3$). (a) Tauc plots with linear fits used to determine the optical bandgap of perovskite photoactive layers. (b) Structure and cross-sectional SEM image of the inverted perovskite solar cells. The false color applied to the SEM image follows the scheme shown in the adjacent schematic. Reverse current−voltage scans under 1 sun illumination applying (c) thin (~350 nm) and (d) thick (500−600 nm) perovskite photoactive layers.

Increasing the open-circuit voltage (V_{oc}) of perovskite devices is essential to progress toward the maximum theoretical single-junction solar cell efficiency limit.[37−40] A widely applied approach to increase V_{oc} is widening the bandgap of the photoactive semiconductor material. According to the Shockley−Queisser limit the maximum single-junction PCE (32−33%) can be achieved with a semiconductor bandgap between 1.2 and 1.4 eV.[41,42] Therefore, widening the bandgap of $MAPbI_3$ (1.6 eV) is predicted to increase V_{oc}, but at the same time a continuous drop in PCE is expected because of the reduced overlap between active layer absorption and the solar spectrum leading to a decrease in the generated short-circuit current density (J_{sc}). Additionally, in most studies an intensified V_{oc} loss is observed with growing bromide content because of increased interfacial and bulk nonradiative recombination.[34,43,44] Despite all of this, some studies have shown that mixed-halide perovskite photoactive layers containing a small amount of bromide (5−15 mol %) with larger bandgap than $MAPbI_3$ itself can enhance, at the same time, both the V_{oc} and PCE of devices.[18,45,46] Interestingly, some of the high-efficiency (PCE > 22%) mixed-cation perovskite devices make use of a mixed-halide photoactive layer with a similar, low (5−10 mol %) bromide content.[47,48] This unexpected increase in device efficiency of low bromide content mixed-halide perovskites still requires clear explanation, especially in terms of a detailed energetic picture.

Valuable information on the energy levels of photoactive perovskite layers and charge extraction interlayers, as well as on the band bending at their interfaces can be achieved by contactless techniques such as ambient photoemission spectroscopy (APS) and surface photovoltage (SPV) measurements. APS has been applied not just to determine the valence band edge (E_v) value of perovskite and organic semiconductor photoactive layers but also to reveal information on relative trap state densities.[49−52] SPV measures the surface potential difference between the dark and under light conditions, which is caused by the photoinduced charge carrier generation and redistribution.[53−55] The redistribution of photogenerated charge carriers is governed by the band bendings (i.e., electric fields) present at the interfaces. Therefore, SPV can provide important information about the internal electric field within semiconductor layer stacks, as well as interfacial charge carrier recombination losses in perovskite solar cells.[56,57]

Herein, we investigate the critical role of a small amount of bromide content (<15 mol %) incorporated into the $MAPbI_3$ perovskite layer. The mixed-halide $MAPb(I_{0.875}Br_{0.125})_3$ in-

https://doi.org/10.1021/acsenergylett.1c02044
ACS Energy Lett. 2021, 6, 3970−3981

Table 1. Average Photovoltaic Performance of $MAPb(I_{1-x}Br_x)_3$ Perovskite Solar Cells Applying Thin (~350 nm) Photoactive Layers[a]

	J_{sc} (mA cm^{-2})	V_{oc} (V)	FF (−)	PCE (%)
x = 0 ($MAPbI_3$)	−19.5 ± 0.1	1.02 ± 0.01	0.75 ± 0.01	15.0 ± 0.1
x = 0.125	−19.8 ± 0.2	1.05 ± 0.01	0.78 ± 0.01	16.1 ± 0.1
x = 0.25	−12.4 ± 0.2	1.12 ± 0.01	0.66 ± 0.02	9.1 ± 0.5
x = 0.50	−6.4 ± 0.2	1.08 ± 0.01	0.58 ± 0.03	4.0 ± 0.1
x = 0.75	−1.9 ± 0.1	0.83 ± 0.02	0.57 ± 0.40	0.9 ± 0.1
x = 1 ($MAPbBr_3$)	−1.1 ± 0.02	0.65 ± 0.02	0.37 ± 0.01	0.3 ± 0.1

[a]The characteristic values were extracted from reverse current−voltage scans.

Table 2. Average Photovoltaic Performance of $MAPb(I_{1-x}Br_x)_3$ Perovskite Solar Cells Applying Optimized Photoactive Layer Thicknesses (500−600 nm)[a]

	J_{sc} (mA cm^{-2})	V_{oc} (V)	FF (−)	PCE (%)
x = 0 ($MAPbI_3$), optimized	−20.7 ± 0.4	1.05 ± 0.01	0.81 ± 0.01	17.5 ± 0.4
x = 0.125, optimized	−21.1 ± 0.4	1.10 ± 0.01	0.81 ± 0.01	18.9 ± 0.3

[a]The characteristic values were extracted from reverse current−voltage scans.

verted structure perovskite solar cells show a high PCE of 19.2% compared to the 18.1% PCE of their $MAPbI_3$ counterparts. We find that with increasing bromide content (x) of $MAPb(I_{1-x}Br_x)_3$ photoactive layers, the optical bandgap increases continuously; however, all energy levels of the x = 0.125 mixed-halide perovskite become significantly shallower (~200 meV) compared to both the x = 0 ($MAPbI_3$) and x = 0.25 perovskite layers. It is found that the x = 0.125 layer has a reduced density of electronic trap states and a tetragonal crystal structure with compressed unit cell, without any measurable signs of halide segregation, which is significantly different from the higher bromide content ($x \geq 0.15$) mixed-halide perovskite layers. We show evidence by SPV measurements that the shallower energy levels of the x = 0.125 perovskite layer allow the elimination of an undesirable interfacial band bending at the hole transport layer (HTL)/perovskite interface that is present in the case of $MAPbI_3$. We conclude that fine-tuning the energy levels of the $MAPbI_3$ perovskite layer, while keeping a stable tetragonal mixed-halide phase (with compressed unit cell), is a key factor achieved by a small amount of bromide incorporation, which leads to the observed enhancement in both V_{oc} and PCE of the solar cells.

Device Performance of Mixed-Halide Photoactive Layers. Mixed-halide perovskite photoactive layers with the composition of $MAPb(I_{1-x}Br_x)_3$ were prepared by increasing the bromide content gradually from x = 0 ($MAPbI_3$) to x = 1 ($MAPBr_3$). The optical bandgap of the mixed-halide semiconductor layers, determined from Tauc plots (Figure 1a), increases monotonically both in the small (x < 0.20, Figure S1) and large bromide content regime, with slight deflection from a linear relationship (Figure S2) in the 1.6−2.3 eV range, which is in good agreement with previous studies.[17−19] These photoactive layers were applied in an inverted structure solar cell containing indium tin oxide (ITO) on glass as a transparent conductive substrate, polytriarylamine (PTAA) with a thin (<10 nm) polymer layer of poly(9,9-bis(3′-(N,N-dimethyl)-N-ethylammoinium-propyl-2,7-fluorene)-*alt*-2,7-(9,9-dioctylfluorene))dibromide (PFN) as hole transport layer, and on top of the perovskite photoactive layer, [6,6]-Phenyl-C61-butyric acid methyl ester (PCBM) as electron transport layer (ETL), a thin (<10 nm) layer of bathocuproine (BCP) and finally evaporated silver (Ag) as top electrode. The schematic structure of the devices, showing all the constituent layers along with the cross-sectional SEM image of a high-performing mixed-halide solar cell, is depicted in Figure 1b.

The devices were prepared first with a thinner (~350 nm) photoactive layer to allow for easier fabrication of reproducible, high-quality perovskite layers, which were also used for the energetic and optoelectronic characterizations. These photoactive layers were then optimized for maximum efficiency by increasing the active layer thickness (500−600 nm).[58] The current−voltage curves of the mixed-halide solar cells displayed in Figure 1c show that the J_{sc} gradually drops with increasing bromide content. This is expected and correlates with the observed increase in the optical bandgap, resulting in reduced harvesting of low-energy photons. On the other hand, the V_{oc} of the $MAPb(I_{1-x}Br_x)_3$ cells increases up to x = 0.25 but significantly decreases when $x \geq 0.5$, indicating the presence of intensifying recombination loss processes possibly because of the growing energetic misalignment with the transport layers.[43] The characteristic values extracted from the current−voltage curves of thin devices (summarized in Table 1) show that interestingly, the highest PCE (16.1%) is observed with the x = 0.125 perovskite layer, which is much larger than the $MAPbI_3$ reference (PCE of 15.0%). This increase in PCE is due to the higher V_{oc} and FF along with the maintained value of J_{sc}. The mixed-halide $MAPb(I_{1-x}Br_x)_3$ perovskite layer producing the highest performance at x = 0.125 composition is in very good agreement with another study observing the same trend with maximum PCE at x = 0.11.[59] This increased PCE of the x = 0.125 mixed-halide layer deviates from the Shockley−Queisser model predicting a decrease in PCE when increasing the bandgap (+60 meV). The observed enhancement of V_{oc} with increasing bromide content is expected as a result of widening semiconductor bandgap (see Figures 1a and S1). However, according to the Shockley−Queisser model, the drop in J_{sc} should dominate and lead to a reduced PCE for the wider bandgap (1.66 eV) photoactive layer.[41,42] This interesting deviation suggests the presence of further, yet unconsidered changes in optoelectronic properties with the incorporation of a small amount of bromide into $MAPbI_3$, which are responsible for the high maintained J_{sc} of the x = 0.125 along with the increased V_{oc}.

Optimized devices with much thicker photoactive layers (Figure 1d) confirm the significantly enhanced average PCE (18.9%) of the x = 0.125 perovskite devices compared to the

https://doi.org/10.1021/acsenergylett.1c02044
ACS Energy Lett. 2021, 6, 3970−3981

$MAPbI_3$ reference (PCE of 17.5%), which is mainly due to a significantly increased V_{oc} (+50 mV) up to 1.10 V with a slightly larger J_{sc} (summarized in Table 2; statistical distribution of characteristic device parameters are compared in Figure S3). The devices showed the same trend for both forward and reverse current−voltage scans with minimal hysteresis (Figure S4 and Table S1). Improved device efficiency compared to $MAPbI_3$ was also observed with even smaller (e.g., x = 0.075) bromide content (see Figure S5 and Table S2); however, the largest V_{oc} increase with maintained high J_{sc}, and resulting highest PCE, was observed at x = 0.125, which puts this composition into the focus of this work. We notice that the optimized device thickness is different for $MAPbI_3$ (~500 nm) and the x = 0.125 mixed-halide perovskite (~600 nm), which agrees with previous studies suggesting defect passivation by bromide incorporation leading to thicker optimized active layer thickness.[59] Importantly, in the thickness range of 500−600 nm the short-circuit current density is expected to be already mostly saturated,[60] and so we consider the contribution from the increased absorption to be minimal. Note that the champion $MAPb(I_{0.875}Br_{0.125})_3$ devices reached a PCE of 19.2% (Figure S6), which is to our knowledge one of the highest values for $MAPb(I_{1-x}Br_x)_3$ solar cells reported in the literature.[45,59,61]

Energy Levels of Mixed-Halide Perovskite Layers. In order to understand the observed unexpected increase of PCE with the x = 0.125 $MAPb(I_{1-x}Br_x)_3$ devices, we performed detailed energy level measurements on all the constituent layers of the inverted structure solar cell and the perovskite photoactive layers (with ~350 nm thickness) covering the full range of mixed-halide compositions. The values of E_v or highest occupied molecular orbital (HOMO) were determined by ambient photoemission spectroscopy (APS), and the Fermi levels (E_F) were taken from the equilibrium dark work function values measured by Kelvin probe. Considering the negligible exciton binding energy at room temperature,[62−64] the conduction band edge (E_c) values of the perovskite layers were calculated by adding the optical bandgap of the semiconductors (Figure 1a) to the measured E_v. The energy band diagrams are displayed in Figure 2 (all energy level values are summarized in Table S2), which show that the HOMO level of the PTAA/PFN HTL (−5.0 eV) is shallower than the E_v of the perovskite layers, forming no energetic barrier for hole transfer from the photoactive layer to the HTL. Similarly, the LUMO of the PCBM ETL (−3.9 eV) is deeper than the E_c of the perovskite layers, allowing a barrier-free electron transfer. The general trend with increasing the bromide content of the $MAPb(I_{1-x}Br_x)_3$ perovskite layers is a deepening of the E_v from −5.4 eV ($MAPbI_3$) to −5.7 eV ($MAPbBr_3$). As the optical bandgap of the mixed-halide perovskites become larger (Figure 1a), the deepening of the E_v is accompanied by E_c becoming shallower in the energy range of −3.8 eV ($MAPbI_3$) to −3.4 eV ($MAPbBr_3$), which is in good agreement with previous studies.[65−67] The growing energetic misalignment between the mixed-halide layers and the transport layers (i.e., increasing difference between the relevant E_v − HOMO and E_c − LUMO energy levels) was shown to lead to reduced device performance and can provide partial explanation for the observed drop in both PCE and V_{oc} for the $x \geq 0.5$ mixed-halide compositions.[68,69]

Interestingly, the energetics of the x = 0.125 $MAPb(I_{1-x}Br_x)_3$ sample is outside the general trend as all energy levels are 200−300 meV shallower compared to the $MAPbI_3$ reference sample. These results reveal a strong correlation between the energy levels and the solar cell performance as the highest PCE (Figure 1) was achieved in this x = 0.125 bromide composition. The HTL deposited under the perovskite absorber layers (both in devices and in the energy level measurements) was dopant-free in order to keep its beneficial effect on reducing interfacial recombination as demonstrated previously.[56,70] The dopant-free nature of the PTAA/PFN layers is reflected in its relatively shallow E_F (−4.7 eV), compared to which all of the $MAPb(I_{1-x}Br_x)_3$ samples showed a deeper E_F (between −4.9 and −5.1 eV) with the exception of the x = 0.125 perovskite layer (E_F of −4.7 eV). This suggests a different band bending at the HTL/perovskite (x = 0.125) interface compared to all the other compositions.

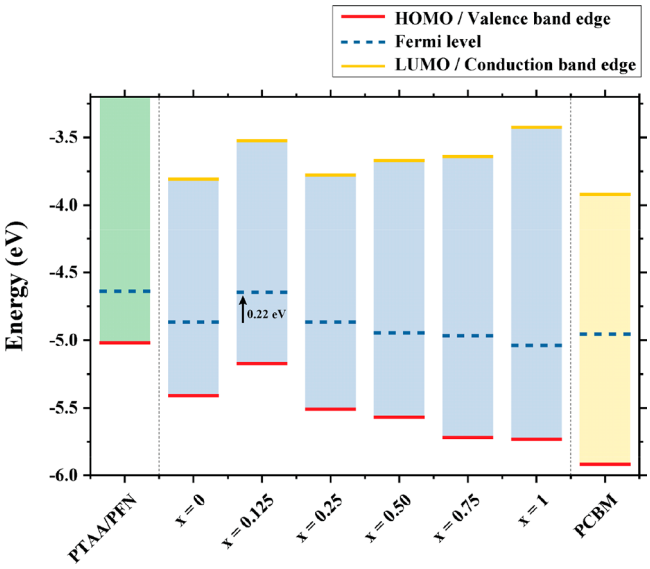

Figure 2. Energy level diagrams for the hole transport layer (green), electron transport layer (yellow), and $MAPb(I_{1-x}Br_x)_3$ perovskite photoactive layers (blue) with different halide composition from x = 0 ($MAPbI_3$) to x = 1 ($MAPbBr_3$).

Trap States and Structural Changes of Mixed-Halide Perovskite Layers. To understand the origin of the high device performance and energetic shift observed with the x = 0.125 perovskite layer we investigate the electronic trap states and associated structural changes of $MAPb(I_{1-x}Br_x)_3$ samples with varying halide content. The cube root photoemission spectra of the mixed-halide layers (with ~350 nm thickness) are shown in Figure 3a with a linear fit used to determine the E_v.[56,57] The photoemission signal measured below the extrapolated E_v (shaded in Figure 3a) indicates the presence of intrabandgap hole trap states in the perovskite layers.[49,50] The relative density of these hole trap states (normalized to $MAPbI_3$) extracted from the APS spectra are compared in Figure 3b for the $MAPb(I_{1-x}Br_x)_3$ layers, revealing a reduced density of trap states with small amounts of bromide incorporation ($x \leq 0.25$) and significantly increased trap densities with larger bromide content. The trap state passivation observed here might indicate a superior perovskite crystal structure with reduced defect density,[59] formed by incorporating a small amount of bromide ($x \leq 0.25$) into $MAPbI_3$, which can contribute to V_{oc} increase in devices. Importantly, the trap state densities of the x = 0.125 and x = 0.25 samples are very similar, while devices with the x = 0.25 photoactive layer show significantly lower J_{sc} and PCE, which

https://doi.org/10.1021/acsenergylett.1c02044
ACS Energy Lett. 2021, 6, 3970−3981

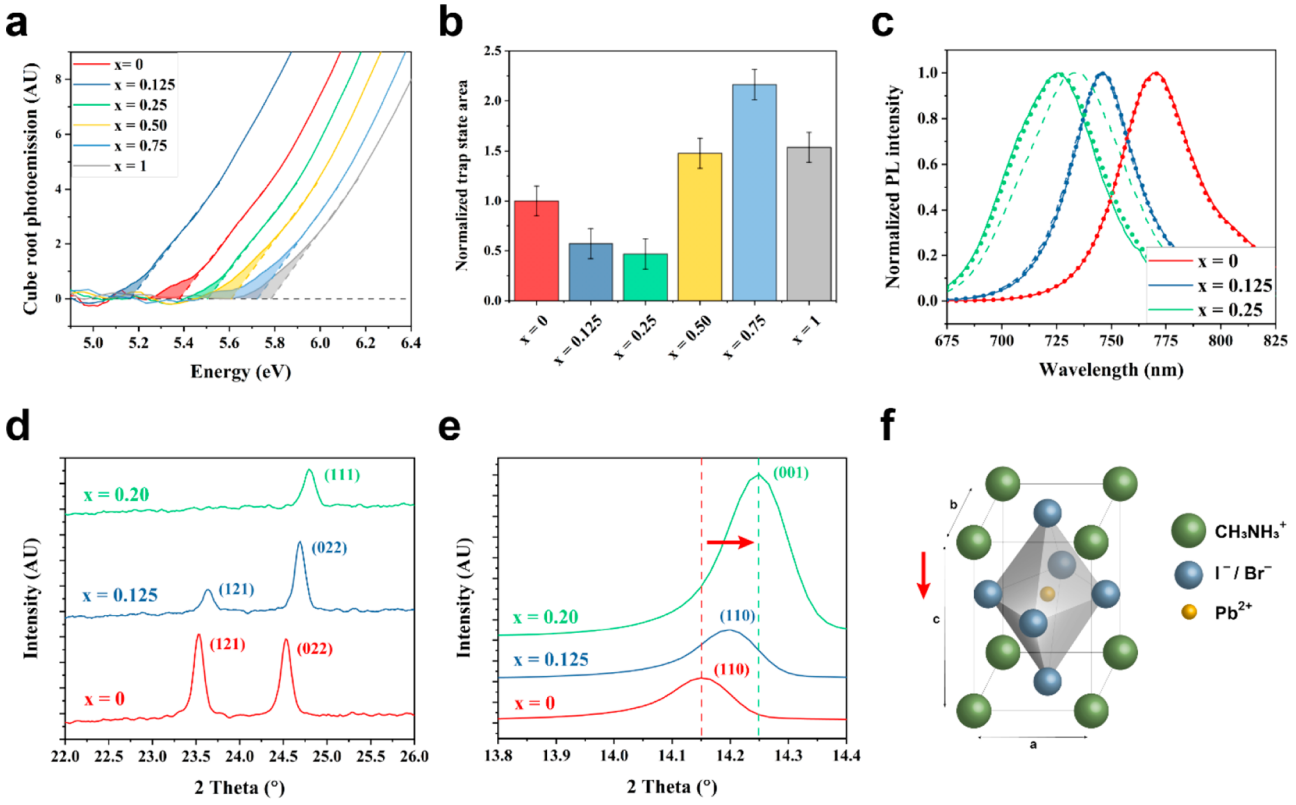

Figure 3. (a) Ambient photoemission spectra of $MAPb(I_{1-x}Br_x)_3$ perovskite photoactive layers with different halide composition from $x = 0$ ($MAPbI_3$) to $x = 1$ ($MAPbBr_3$) showing the linear fit used to determine the valence band edge. The shaded parts of the spectra represent trap states below the valence band edge. (b) Comparison of trap state related areas normalized to $MAPbI_3$ ($x = 0$). (c) Normalized PL spectra of $MAPb(I_{1-x}Br_x)_3$ perovskite layers with low bromide content ($x \leq 0.25$) measured initially (solid lines), after 5 min light soaking (dashed lines), and after 10 min dark recovery (dotted lines, overlapping with initial solid lines). X-ray diffractograms comparing the (d) (121), (022) and (e) (110) diffraction peaks. (f) Tetragonal perovskite crystal structure indicating with red arrow the change in lattice constant with increasing bromide content.

suggests that other factors likely play a more significant role. In contrast, the larger trap state densities measured in the higher bromide content ($x > 0.25$) mixed-halide samples provide a plausible reason for the observed V_{oc} loss (Figure 1c), possibly by increased trap-assisted nonradiative recombination.[71,72]

Different from the beneficial effects of incorporating a small amount of bromide ($x = 0.125$), mixing more ($x = 0.25$) into $MAPbI_3$ induces a large drop in J_{sc} (and associated PCE). In order to understand this, we carried out further examinations of perovskite crystal structures and their phase changes under dark and light conditions. The initial photoluminescence (PL) spectra of the low bromide content ($x = 0.125$ and 0.25) $MAPb(I_{1-x}Br_x)_3$ perovskite layers show a blue-shift in the peak position (see Figure 3c) from 770 nm ($x = 0$) to 746 nm ($x = 0.125$) and 726 nm ($x = 0.25$) as a result of the increased bandgap. After 5 min of illumination, the peak position of the $x = 0.25$ perovskite layer red-shifted by 7 nm (dashed lines in Figure 3c) but fully recovered to its initial position after 15 min in the dark (dotted lines in Figure 3c, overlapping with initial solid lines), both of which have been reported as signatures of light-induced halide demixing.[26,27] This phase-segregation related phenomenon was clearly present for all higher bromide content mixed-halide perovskite samples as well (Figure S7). Strikingly, the first signs of such peak shifts were observable at $x = 0.15$ (2 nm peak shift, see Figure S8) but did not appear at all for the $x = 0.125$ perovskite layer. This result indicates a stable crystalline structure of the $x = 0.125$ mixed-halide layer, not being subject to light-induced halide phase-segregation, which correlates well with its high device performance. These results are also in good agreement with other studies suggesting that the vacancy-assisted ion migration induces halide segregation, contributing to degradation of device performance,[73−76] as found here with the high bromide content samples.

Structural analysis by XRD reveals that $MAPbI_3$ ($x = 0$) exists in the tetragonal phase, evidenced by the (121) diffraction peak observed at 23.5° 2θ (Figure 3d, see full spectra in Figure S9).[46,77] Another signature of the tetragonal phase is its transition to orthorhombic phase between 130 and 150 K that is observed for the $MAPbI_3$ reference sample in temperature-dependent PL measurements (Figure S10).[78,79] Importantly, both the (121) diffraction peak at 23.5° 2θ and the PL transition temperature around 140 K are observed for the $x = 0.125$ perovskite sample; however, neither are present for the higher bromide content ($x \geq 0.20$) mixed-halide samples (see Figure 3d for XRD and Figure S10 for temperature-dependent PL signals).

The decrease in the relative intensity of the (121) diffraction peak relative to the (022) diffraction peak when the composition changes from $x = 0$ to $x = 0.125$ is also accompanied by a shift of the (110) diffraction peak at 14.15° 2θ to higher angles (see Figure 3e). This translates to the reduction of unit cell volume with increasing bromide content, as illustrated in Figure 3f. Such compression of unit cell

https://doi.org/10.1021/acsenergylett.1c02044
ACS Energy Lett. 2021, 6, 3970−3981

volume has been correlated to a reduced density of trap states,[80,81] which is in excellent agreement with the decreased trap state density measured by APS for the small bromide content ($x \leq 0.25$) perovskite samples (see Figure 3b). It seems, however, that the positive effect of the crystal structure change on device efficiency holds only while the perovskite layer is in the tetragonal phase ($x \leq 0.125$), after which halide segregation starts to dominate. This hypothesis is supported when considering the best performing (highest perovskite layer quality) $x = 0.125$ composition showing minimal reduction in the (121) diffraction peak intensity (Figure S11), i.e., maintaining the tetragonal crystal phase, but with reduced unit cell volume, which is a plausible explanation for the observed energetic shift toward shallower energy levels (Figure 2). It has been shown that increasing the crystal symmetry (i.e., transition from tetragonal to cubic phase) can reduce ion migration activation energy,[75,82,83] rationalizing the importance of the tetragonal phase in the context of halide segregation. Interestingly, a similar relationship between changing perovskite crystal structure and halide segregation appearing only at a certain composition was also observed in triple halide perovskite studies.[84]

Scanning electron microscopy (SEM) images show similar coverage and grain size (200−300 nm) for both $MAPbI_3$ and $MAPb(I_{0.875}Br_{0.125})_3$ layers (see Figure S12), while the root-mean-square (RMS) roughness measured by atomic force microscopy (AFM) is slightly reduced (see Figure S13 and Table S4) for the low bromide content ($x \leq 0.125$) layers (8.3 ± 0.7 nm) compared to $MAPbI_3$ (9.5 ± 0.5 nm). However, further increasing the bromide content of the mixed-halide perovskite layers results in a significantly larger RMS roughness (12.3−27.2 nm), confirming a less desirable morphology with higher bromide ratios ($x \geq 0.15$).

Surface Photovoltage of Mixed-Halide Perovskite Layers. After gaining insight into structural and energetic changes of the $MAPb(I_{1-x}Br_x)_3$ perovskite layers, both showing distinctive characteristics at the $x = 0.125$ composition, the relation between the observed energy level changes and device performance is investigated further by SPV and alternating current surface photovoltage (AC-SPV) measurements. The difference between the signal generation of the two Kelvin probe-based techniques is illustrated in Scheme 1.

When a Kelvin probe is used to determine the work function of a semiconductor sample, the voltage signal is typically generated by a vibrating (here ∼80 Hz) metal tip modulating the capacitance between the tip and the grounded sample.[85,86] In the case of SPV, the surface potential in the dark (WF_{dark}) and under illumination (WF_{ill}) is measured, and their difference is calculated: $SPV = WF_{ill} - WF_{dark}$. Note that work function and Fermi level are defined under dark, equilibrium conditions; hence, WF_{ill} is referred to as surface potential under illumination. The voltage signal (see Scheme 1) is generated by a vibrating KP tip (i.e., by the periodic sinusoidal displacement of the tip varying the capacitance via changing the tip−sample distance). Measuring the peak-to-peak values of the voltage signal under different applied backing voltages allows for the determination of the surface potential of the sample. The surface potential can be obtained in this way both in the dark and under illumination (contrary to AC-SPV), enabling the recording of their difference (i.e., SPV), as well as the turn-on and -off SPV dynamics.

Scheme 1. Schematic Representation and Experimental Timelines of Signal Generation Comparing Surface Photovoltage (SPV) and Alternating Current Surface Photovoltage (AC-SPV)

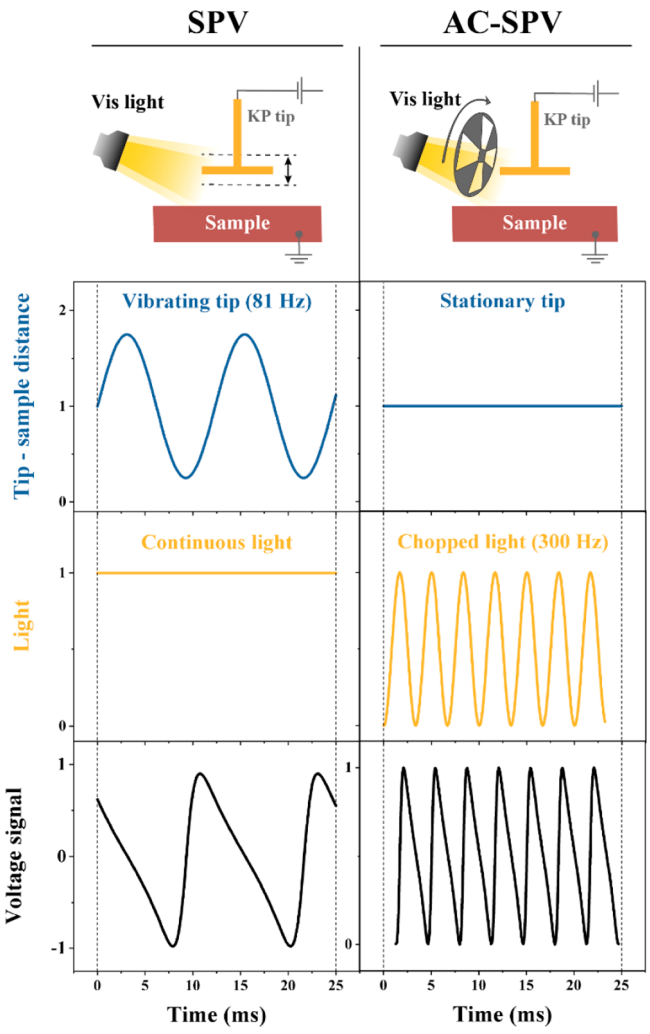

In contrast, AC-SPV applies chopped light with a certain frequency (here ∼300 Hz), while the Kelvin probe tip is kept stationary.[87,88] The voltage signal for AC-SPV signal is generated by the chopped light modulating the surface potential of the sample and by that creating an AC current between the tip and the sample. This means that there is no reference potential measured in the dark, only a potential difference (peak-to-peak value of the sinusoidal voltage signal) under AC-modulated incident light. In both SPV and AC-SPV the redistribution of the photogenerated charge carriers is necessary to observe a signal, which is governed by the band bendings (i.e., electric fields) present in the semiconductor layer.[53,56] However, for a significant AC-SPV signal (i.e., large peak-to-peak value for the voltage signal) to be observed, both a relatively fast charge generation and redistribution under illumination and a quick recombination (and/or redistribution) of charge carriers in dark conditions is necessary.[89,90] Therefore, SPV measurements can track the slow (seconds time scale) surface potential changes under illumination such as ion migration in perovskites, while AC-SPV is better suited to investigate faster processes on the time scale of the light modulation frequency (here, ∼3 ms). This makes AC-SPV a

https://doi.org/10.1021/acsenergylett.1c02044
ACS Energy Lett. 2021, 6, 3970−3981

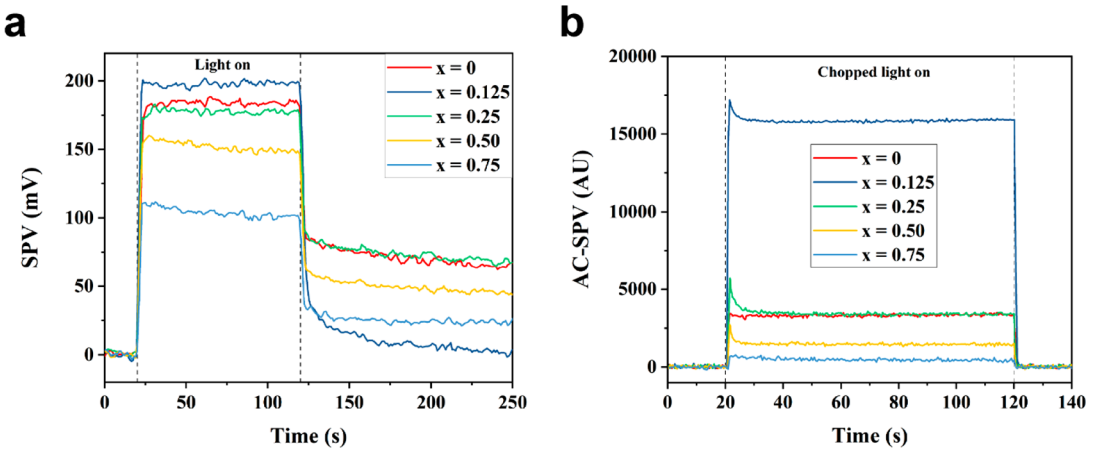

Figure 4. (a) Surface photovoltage (SPV) and (b) alternating current surface photovoltage (AC-SPV) signals of $MAPb(I_{1-x}Br_x)_3$ perovskite photoactive layers with different halide composition deposited on ITO/PTAA/PFN hole transport layer. Dashed vertical lines indicate when the light was turned on (first line) and off (second line).

Scheme 2. Energy Band Diagrams Showing Surface Photovoltage (SPV) Generation for (a) $x = 0$ ($MAPbI_3$) (SPV_1) and (b) $x = 0.125$ $MAPb(I_{1-x}Br_x)_3$ (SPV_2) Thin Films Deposited on ITO/PTAA/PFN Hole Transport Layer[a]

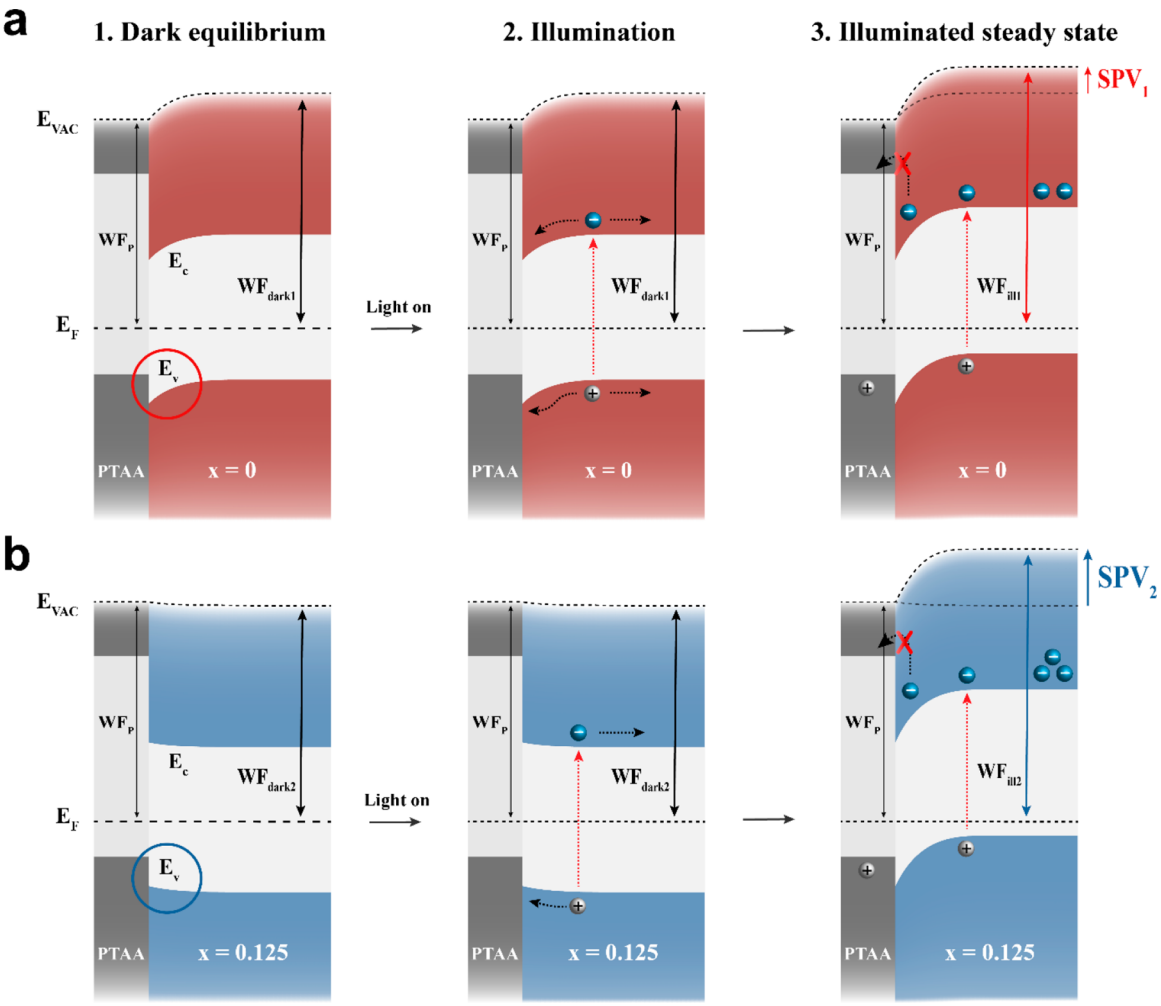

[a]For simplification, only one underlayer, labelled PTAA, is shown. WF_P denotes the work function of the ITO/PTAA/PFN underlayer, while WF_{dark1}, WF_{ill1}, WF_{dark2}, and WF_{ill2} are the measured surface potential of $MAPbI_3$ and $MAPb(I_{0.875}Br_{0.125})_3$ in dark and at illuminated steady state, respectively. The middle diagrams show the first moment of charge-carrier generation by light absorption (red dotted lines) and charge transport (by drift closer to the interface and diffusion in the bulk) indicated by black arrows. The vacuum level, Fermi level, valence band edge, and conduction band edges are denoted by E_{vac} (dotted line), E_F (dashed line), E_v, and E_c, respectively. Electrons and holes are represented by circles with negative and positive signs, respectively.

https://doi.org/10.1021/acsenergylett.1c02044
ACS Energy Lett. 2021, 6, 3970−3981

useful tool to study the faster electronic processes in perovskites separate from the slower ionic contributions.

The SPV signal of the $MAPb(I_{1-x}Br_x)_3$ perovskite layers deposited on PTAA/PFN HTLs show a positive sign in all cases (Figure 4a), confirming the anticipated increased density of electrons at the surface of the samples.[56,57] The magnitude of SPV for the $MAPbI_3$ reference (185 mV) increases (to 200 mV) at $x = 0.125$; however, it drops gradually (to 100−180 mV) for the higher bromide content mixed-halide samples ($x \geq 0.25$). The significant variation in SPV magnitude suggests a change in band bending at the HTL/$MAPb(I_{1-x}Br_x)_3$ interface with different halide contents. Note that if there was a change in the surface (i.e., perovskite/air interface) band bending between the mixed-halide layers, a smaller SPV value would be expected[49,91] for the $MAPb(I_{0.875}Br_{0.125})_3$ sample with fewer surface trap states compared to $MAPbI_3$; however, the opposite is observed.

The change in interfacial band bending is expected considering the E_F alignment between the PTAA/PFN HTL and the mixed-halide photoactive layers: the E_F of $MAPbI_3$ lies deeper that of the HTL, generating an upward band bending toward the surface after E_F alignment, as illustrated in Scheme 2a. This upward (toward the surface) band bending represents an undesirable electric field as it drives photogenerated electrons toward the HTL and its effect becomes larger as the E_F of the $MAPb(I_{1-x}Br_x)_3$ layers get deeper ($x \geq 0.25$). The positive SPV signal for these layers (see Figure 4a) is due to the blocking property of the HTL, which extracts holes selectively, resulting in an increased density of electrons in the perovskite layer. Such an electron-blocking property of the HTL is that allows for the band bending to extend beyond the flat band condition. However, the large upward (toward the surface) band bending at the HTL/$MAPbI_3$ interface clearly limits the SPV magnitude as well as the linked device performance. In contrast, with the 200 meV shallower E_F of the ($x = 0.125$) perovskite layer the same amount of change in band bending is expected, and so the undesired interfacial band bending can be eliminated as illustrated in Scheme 2b, allowing for a more efficient separation and transport of electrons and holes at the HTL/perovskite interface, thereby enabling the generation of a larger SPV and in devices a higher performance.

The SPV turn-on response times are relatively fast in all cases; however, on the normalized SPV signals (Figure S14) it is observed that the $x = 0.125$ composition shows a slightly faster SPV turn-on as the interfacial electric field helps charge extraction, compared to $MAPbI_3$. When the light is turned off there is a quick drop in the SPV signal for all samples; however, there is still an offset present and SPV decays back slowly, on the seconds time scale, to its initial dark equilibrium value. This slow decay after illumination is turned off was linked to slow ion migration and trapped charge carriers in the perovskite layer,[56,92−94] which can explain the significantly lower SPV offset of the $x = 0.125$ perovskite layer with more perfect crystal structure and reduced trap density compared to $MAPbI_3$.

The AC-SPV signals of the mixed-halide samples (Figure 4b) show the same trend as SPV, but the differences in AC-SPV values are even larger. This is due to AC-SPV measuring mainly the faster electronic charge carriers, without the effects of slow ion movement, making the technique more sensitive to the changes in internal electric field within the sample. The AC-SPV magnitudes of the $MAPb(I_{1-x}Br_x)_3$ layers follow the same trend as the E_F: the $x = 0.125$ sample with 200 meV shallower E_F generates more than three times larger AC-SPV signal compared to the reference ($x = 0$) and the $x = 0.25$ sample, both of which show exactly the same deeper E_F (−4.88 eV) as well as the same magnitude of AC-SPV signal. Further deepening of the E_F ($x \geq 0.25$) results in significant drop (more than 50%) in the magnitude of AC-SPV signal compared to the $x = 0$ and $x = 0.25$ samples. This striking correlation between the E_F of the $MAPb(I_{1-x}Br_x)_3$ layers and the AC-SPV magnitudes provides strong evidence for the electronic charge carrier separation and transport being determined by the band bending at the HTL/$MAPb(I_{1-x}Br_x)_3$ interface with varying bromide content (see Scheme 2). The largest AC-SPV (and SPV) signals of the $x = 0.125$ mixed-halide layer suggests the presence of optimal interfacial band bending. Together with stable crystalline structure against halide segregation and reduced trap states, the $x = 0.125$ mixed-halide layer provides an effective way to tune the energetics and through that the interfacial band bending to achieve more efficient charge extraction. This is also well aligned with faster transient photocurrents reported using a similar composition ($x = 0.11$) mixed-halide layer.[59] Finally, the increased efficiency of charge transport enabled by the modified interfacial band bending provides explanation for the simultaneously enhanced V_{oc} and PCE of the $x = 0.125$ $MAPb(I_{1-x}Br_x)_3$ perovskite solar cells.

In summary, $MAPb(I_{1-x}Br_x)_3$ mixed-halide perovskite photoactive layers were investigated in inverted structure solar cells, and a peak efficiency (PCE of 19.2%) was found at low bromide content ($x = 0.125$), despite the large bandgap (1.66 eV) of the absorber. The analysis of the energetics revealed a deepening of the E_F and the E_v with increasing bromide ratio ($x \geq 0.25$), except for the high performing $x = 0.125$ perovskite layer possessing 200 meV shallower energy levels compared to $MAPbI_3$. It was found that incorporation of a small amount of bromide content reduces the density of hole traps and it compresses the unit cell of the mixed-halide perovskites, which have a positive effect on the crystalline and electronic quality of the photoactive layer. Importantly, the $x = 0.125$ perovskite layer shows no signs of halide segregation. The composition where the phase segregation related redshift in PL is first observable ($x \geq 0.15$) coincides with the disappearance of the tetragonal perovskite crystal phase, evidenced by XRD and temperature-dependent PL measurements. This shows that the shallower energetics of the $x = 0.125$ mixed-halide layer is linked to a compressed perovskite structure with reduced density of defect states compared to $MAPbI_3$, which is stable as it is still mostly in the tetragonal crystal phase. SPV and AC-SPV measurements revealed that the deep E_F of the $MAPb(I_{1-x}Br_x)_3$ layers ($x = 0$ and $x \geq 0.25$) is the origin of an undesirable upward (toward the surface) interfacial band bending at the HTL/perovskite interface, reducing device performance. In contrast, the shallower energy levels of the $x = 0.125$ perovskite layer provide a way to eliminate this hindering interfacial band bending, thus increasing the efficiency of charge extraction and allowing for the observed enhancement of PCE. These findings give detailed insight into the energetic and structural origin of the peculiar solar cell efficiency increase of the $MAPb(I_{1-x}Br_x)_3$ perovskite solar cells containing a small amount of bromide ($x = 0.125$). These results also highlight the important role of energetics and interfacial band bending in perovskite solar

https://doi.org/10.1021/acsenergylett.1c02044
ACS Energy Lett. 2021, 6, 3970−3981

cells, showing that their careful tuning is essential and a successful way to increase their device efficiency.

■ ASSOCIATED CONTENT

Supporting Information

The Supporting Information is available free of charge at https://pubs.acs.org/doi/10.1021/acsenergylett.1c02044.

Experimental details; Tauc plots; solar cell device performance data and statistics; energetic, PL, XRD, SEM, and AFM plots and data (PDF)

■ AUTHOR INFORMATION

Corresponding Author

Ji-Seon Kim − *Department of Physics and Centre for Processable Electronics, Imperial College London, London SW7 2AZ, U.K.;* orcid.org/0000-0003-4715-3656; Email: ji-seon.kim@imperial.ac.uk

Authors

Matyas Daboczi − *Department of Physics and Centre for Processable Electronics, Imperial College London, London SW7 2AZ, U.K.;* orcid.org/0000-0001-9920-3657

Sinclair R. Ratnasingham − *Department of Materials and Centre for Processable Electronics, Imperial College London, London SW7 2AZ, U.K.*

Lokeshwari Mohan − *Department of Materials and Centre for Processable Electronics, Imperial College London, London SW7 2AZ, U.K.*

Chenfeng Pu − *Department of Physics and Centre for Processable Electronics, Imperial College London, London SW7 2AZ, U.K.*

Iain Hamilton − *Division of Physical Sciences and Engineering, King Abdullah University of Science and Technology (KAUST), Thuwal 23955-6900, Saudi Arabia;* orcid.org/0000-0002-0685-1696

Yi-Chun Chin − *Department of Physics and Centre for Processable Electronics, Imperial College London, London SW7 2AZ, U.K.*

Martyn A. McLachlan − *Department of Materials and Centre for Processable Electronics, Imperial College London, London SW7 2AZ, U.K.;* orcid.org/0000-0003-3136-1661

Complete contact information is available at: https://pubs.acs.org/10.1021/acsenergylett.1c02044

Notes

The authors declare no competing financial interest.

■ ACKNOWLEDGMENTS

The authors acknowledge the funding of UK Engineering and Physical Sciences Research Council (EPSRC) Plastic Electronics Doctoral Training Centre (EP/L016702/1) and KP Technology Ltd for EPSRC CASE studentships. This research was also supported by the UK EPSRC ATIP Programme Grant (EP/T028513/1) and the Global Research Laboratory Program of the National Research Foundation (NRF) funded by the Ministry of Science, ICT & Future Planning (NRF-2017K1A1A2 013153).

■ REFERENCES

(1) Kojima, A.; Teshima, K.; Shirai, Y.; Miyasaka, T. Organometal Halide Perovskites as Visible-Light Sensitizers for Photovoltaic Cells. *J. Am. Chem. Soc.* **2009**, *131* (17), 6050−6051.

(2) Lee, M. M.; Teuscher, J.; Miyasaka, T.; Murakami, T. N.; Snaith, H. J. Efficient Hybrid Solar Cells Based on Meso-Superstructured Organometal Halide Perovskites. *Science (Washington, DC, U. S.)* **2012**, *338* (6107), 643−647.

(3) Eperon, G. E.; Burlakov, V. M.; Docampo, P.; Goriely, A.; Snaith, H. J. Morphological Control for High Performance, Solution-Processed Planar Heterojunction Perovskite Solar Cells. *Adv. Funct. Mater.* **2014**, *24* (1), 151−157.

(4) Ball, J. M.; Lee, M. M.; Hey, A.; Snaith, H. J. Low-Temperature Processed Meso-Superstructured to Thin-Film Perovskite Solar Cells. *Energy Environ. Sci.* **2013**, *6* (6), 1739−1743.

(5) Jeon, N. J.; Noh, J. H.; Yang, W. S.; Kim, Y. C.; Ryu, S.; Seo, J.; Seok, S. Il. Compositional Engineering of Perovskite Materials for High-Performance Solar Cells. *Nature* **2015**, *517* (7535), 476−480.

(6) Saliba, M.; Matsui, T.; Seo, J. Y.; Domanski, K.; Correa-Baena, J. P.; Nazeeruddin, M. K.; Zakeeruddin, S. M.; Tress, W.; Abate, A.; Hagfeldt, A.; Grätzel, M. Cesium-Containing Triple Cation Perovskite Solar Cells: Improved Stability, Reproducibility and High Efficiency. *Energy Environ. Sci.* **2016**, *9* (6), 1989−1997.

(7) Alharbi, E. A.; Alyamani, A. Y.; Kubicki, D. J.; Uhl, A. R.; Walder, B. J.; Alanazi, A. Q.; Luo, J.; Burgos-Caminal, A.; Albadri, A.; Albrithen, H.; Alotaibi, M. H.; Moser, J. E.; Zakeeruddin, S. M.; Giordano, F.; Emsley, L.; Grätzel, M. Atomic-Level Passivation Mechanism of Ammonium Salts Enabling Highly Efficient Perovskite Solar Cells. *Nat. Commun.* **2019**, *10* (1), 1−9.

(8) Bai, S.; Da, P.; Li, C.; Wang, Z.; Yuan, Z.; Fu, F.; Kawecki, M.; Liu, X.; Sakai, N.; Wang, J. T. W.; Huettner, S.; Buecheler, S.; Fahlman, M.; Gao, F.; Snaith, H. J. Planar Perovskite Solar Cells with Long-Term Stability Using Ionic Liquid Additives. *Nature* **2019**, *571* (7764), 245−250.

(9) Jung, E. H.; Jeon, N. J.; Park, E. Y.; Moon, C. S.; Shin, T. J.; Yang, T. Y.; Noh, J. H.; Seo, J. Efficient, Stable and Scalable Perovskite Solar Cells Using Poly(3-Hexylthiophene). *Nature* **2019**, *567* (7749), 511−515.

(10) Zheng, X.; Hou, Y.; Bao, C.; Yin, J.; Yuan, F.; Huang, Z.; Song, K.; Liu, J.; Troughton, J.; Gasparini, N.; Zhou, C.; Lin, Y.; Xue, D. J.; Chen, B.; Johnston, A. K.; Wei, N.; Hedhili, M. N.; Wei, M.; Alsalloum, A. Y.; Maity, P.; Turedi, B.; Yang, C.; Baran, D.; Anthopoulos, T. D.; Han, Y.; Lu, Z. H.; Mohammed, O. F.; Gao, F.; Sargent, E. H.; Bakr, O. M. Managing Grains and Interfaces via Ligand Anchoring Enables 22.3%-Efficiency Inverted Perovskite Solar Cells. *Nat. Energy* **2020**, *5* (2), 131−140.

(11) National Renewable Energy Laboratory. *Best Research-Cell Efficiencies* https://www.nrel.gov/pv/assets/pdfs/best-research-cell-efficiencies.20200104.pdf.

(12) Bi, D.; Tress, W.; Dar, M. I.; Gao, P.; Luo, J.; Renevier, C.; Schenk, K.; Abate, A.; Giordano, F.; Correa Baena, J. P.; Decoppet, J. D.; Zakeeruddin, S. M.; Nazeeruddin, M. K.; Grätzel, M.; Hagfeldt, A. Efficient Luminescent Solar Cells Based on Tailored Mixed-Cation Perovskites. *Sci. Adv.* **2016**, *2* (1), e1501170−e1501171.

(13) Yang, Z.; Rajagopal, A.; Jen, A. K. Y. Ideal Bandgap Organic−Inorganic Hybrid Perovskite Solar Cells. *Adv. Mater.* **2017**, *29* (47), 1704418.

(14) Prakash, J.; Singh, A. A.; Sathiyan, G.; Ranjan, R.; Singh, A. A.; Garg, A.; Gupta, R. K. Progress in Tailoring Perovskite Based Solar Cells through Compositional Engineering: Materials Properties, Photovoltaic Performance and Critical Issues. *Mater. Today Energy* **2018**, *9*, 440−486.

(15) Leijtens, T.; Bush, K. A.; Prasanna, R.; McGehee, M. D. Opportunities and Challenges for Tandem Solar Cells Using Metal Halide Perovskite Semiconductors. *Nat. Energy* **2018**, *3* (10), 828−838.

(16) McMeekin, D. P.; Mahesh, S.; Noel, N. K.; Klug, M. T.; Lim, J. C.; Warby, J. H.; Ball, J. M.; Herz, L. M.; Johnston, M. B.; Snaith, H. J. Solution-Processed All-Perovskite Multi-Junction Solar Cells. *Joule* **2019**, *3* (2), 387−401.

(17) Eperon, G. E.; Stranks, S. D.; Menelaou, C.; Johnston, M. B.; Herz, L. M.; Snaith, H. J. Formamidinium Lead Trihalide: A Broadly

Tunable Perovskite for Efficient Planar Heterojunction Solar Cells. *Energy Environ. Sci.* **2014**, *7* (3), 982−988.
(18) Noh, J. H.; Im, S. H.; Heo, J. H.; Mandal, T. N.; Seok, S. Il. Chemical Management for Colorful, Efficient, and Stable Inorganic-Organic Hybrid Nanostructured Solar Cells. *Nano Lett.* **2013**, *13* (4), 1764−1769.
(19) Gil-Escrig, L.; Miquel-Sempere, A.; Sessolo, M.; Bolink, H. J. Mixed Iodide-Bromide Methylammonium Lead Perovskite-Based Diodes for Light Emission and Photovoltaics. *J. Phys. Chem. Lett.* **2015**, *6* (18), 3743−3748.
(20) Zhang, W.; Saliba, M.; Moore, D. T.; Pathak, S. K.; Hörantner, M. T.; Stergiopoulos, T.; Stranks, S. D.; Eperon, G. E.; Alexander-Webber, J. A.; Abate, A.; Sadhanala, A.; Yao, S.; Chen, Y.; Friend, R. H.; Estroff, L. A.; Wiesner, U.; Snaith, H. J. Ultrasmooth Organic-Inorganic Perovskite Thin-Film Formation and Crystallization for Efficient Planar Heterojunction Solar Cells. *Nat. Commun.* **2015**, *6*, 6142.
(21) Ibrahim Dar, M.; Abdi-Jalebi, M.; Arora, N.; Moehl, T.; Grätzel, M.; Nazeeruddin, M. K. Understanding the Impact of Bromide on the Photovoltaic Performance of CH3NH3PbI3 Solar Cells. *Adv. Mater.* **2015**, *27* (44), 7221−7228.
(22) Li, D.; Wang, G.; Cheng, H.-C.; Chen, C.-Y.; Wu, H.; Liu, Y.; Huang, Y.; Duan, X. Size-Dependent Phase Transition in Methylammonium Lead Iodide Perovskite Microplate Crystals. *Nat. Commun.* **2016**, *7* (1), 11330.
(23) Quarti, C.; Mosconi, E.; Ball, J. M.; D'Innocenzo, V.; Tao, C.; Pathak, S.; Snaith, H. J.; Petrozza, A.; De Angelis, F. Structural and Optical Properties of Methylammonium Lead Iodide across the Tetragonal to Cubic Phase Transition: Implications for Perovskite Solar Cells. *Energy Environ. Sci.* **2016**, *9* (1), 155−163.
(24) Byun, H. R.; Park, D. Y.; Oh, H. M.; Namkoong, G.; Jeong, M. S. Light Soaking Phenomena in Organic-Inorganic Mixed Halide Perovskite Single Crystals. *ACS Photonics* **2017**, *4* (11), 2813−2820.
(25) Lehmann, F.; Franz, A.; Többens, D. M.; Levcenco, S.; Unold, T.; Taubert, A.; Schorr, S. The Phase Diagram of a Mixed Halide (Br, I) Hybrid Perovskite Obtained by Synchrotron X-Ray Diffraction. *RSC Adv.* **2019**, *9* (20), 11151−11159.
(26) Hoke, E. T.; Slotcavage, D. J.; Dohner, E. R.; Bowring, A. R.; Karunadasa, H. I.; McGehee, M. D. Reversible Photo-Induced Trap Formation in Mixed-Halide Hybrid Perovskites for Photovoltaics. *Chem. Sci.* **2015**, *6* (1), 613−617.
(27) Draguta, S.; Sharia, O.; Yoon, S. J.; Brennan, M. C.; Morozov, Y. V.; Manser, J. M.; Kamat, P. V.; Schneider, W. F.; Kuno, M. Rationalizing the Light-Induced Phase Separation of Mixed Halide Organic-Inorganic Perovskites. *Nat. Commun.* **2017**, *8* (1), 200.
(28) Bischak, C. G.; Hetherington, C. L.; Wu, H.; Aloni, S.; Ogletree, D. F.; Limmer, D. T.; Ginsberg, N. S. Origin of Reversible Photoinduced Phase Separation in Hybrid Perovskites. *Nano Lett.* **2017**, *17* (2), 1028−1033.
(29) Elmelund, T.; Seger, B.; Kuno, M.; Kamat, P. V. How Interplay between Photo and Thermal Activation Dictates Halide Ion Segregation in Mixed Halide Perovskites. *ACS Energy Lett.* **2020**, *5* (1), 56−63.
(30) McMeekin, D. P.; Sadoughi, G.; Rehman, W.; Eperon, G. E.; Saliba, M.; Hörantner, M. T.; Haghighirad, A.; Sakai, N.; Korte, L.; Rech, B.; Johnston, M. B.; Herz, L. M.; Snaith, H. J. A Mixed-Cation Lead Mixed-Halide Perovskite Absorber for Tandem Solar Cells. *Science (Washington, DC, U. S.)* **2016**, *351* (6269), 151−155.
(31) Sutter-Fella, C. M.; Ngo, Q. P.; Cefarin, N.; Gardner, K. L.; Tamura, N.; Stan, C. V.; Drisdell, W. S.; Javey, A.; Toma, F. M.; Sharp, I. D. Cation-Dependent Light-Induced Halide Demixing in Hybrid Organic-Inorganic Perovskites. *Nano Lett.* **2018**, *18* (6), 3473−3480.
(32) Correa-Baena, J. P.; Luo, Y.; Brenner, T. M.; Snaider, J.; Sun, S.; Li, X.; Jensen, M. A.; Hartono, N. T. P.; Nienhaus, L.; Wieghold, S.; Poindexter, J. R.; Wang, S.; Meng, Y. S.; Wang, T.; Lai, B.; Holt, M. V.; Cai, Z.; Bawendi, M. G.; Huang, L.; Buonassisi, T.; Fenning, D. P.; Holt, V. M.; Cai, Z.; Bawendi, M. G.; Huang, L.; Buonassisi, T.; Fenning, D. P. Homogenized Halides and Alkali Cation Segregation in Alloyed Organic-Inorganic Perovskites. *Science (Washington, DC, U. S.)* **2019**, *363* (6427), 627−631.
(33) Bush, K. A.; Frohna, K.; Prasanna, R.; Beal, R. E.; Leijtens, T.; Swifter, S. A.; McGehee, M. D. Compositional Engineering for Efficient Wide Band Gap Perovskites with Improved Stability to Photoinduced Phase Segregation. *ACS Energy Lett.* **2018**, *3* (2), 428−435.
(34) Mahesh, S.; Ball, J. M.; Oliver, R. D. J. J.; McMeekin, D. P.; Nayak, P. K.; Johnston, M. B.; Snaith, H. J. Revealing the Origin of Voltage Loss in Mixed-Halide Perovskite Solar Cells. *Energy Environ. Sci.* **2020**, *13* (1), 258−267.
(35) Knight, A. J.; Wright, A. D.; Patel, J. B.; McMeekin, D. P.; Snaith, H. J.; Johnston, M. B.; Herz, L. M. Electronic Traps and Phase Segregation in Lead Mixed-Halide Perovskite. *ACS Energy Lett.* **2019**, *4* (1), 75−84.
(36) Barker, A. J.; Sadhanala, A.; Deschler, F.; Gandini, M.; Senanayak, S. P.; Pearce, P. M.; Mosconi, E.; Pearson, A. J.; Wu, Y.; Srimath Kandada, A. R.; Leijtens, T.; De Angelis, F.; Dutton, S. E.; Petrozza, A.; Friend, R. H. Defect-Assisted Photoinduced Halide Segregation in Mixed-Halide Perovskite Thin Films. *ACS Energy Lett.* **2017**, *2* (6), 1416−1424.
(37) Correa-Baena, J. P.; Abate, A.; Saliba, M.; Tress, W.; Jesper Jacobsson, T.; Grätzel, M.; Hagfeldt, A. The Rapid Evolution of Highly Efficient Perovskite Solar Cells. *Energy Environ. Sci.* **2017**, *10* (3), 710−727.
(38) Tress, W. Perovskite Solar Cells on the Way to Their Radiative Efficiency Limit − Insights Into a Success Story of High Open-Circuit Voltage and Low Recombination. *Adv. Energy Mater.* **2017**, *7* (14), 1602358.
(39) Tress, W. Maximum Efficiency and Open-Circuit Voltage of Perovskite Solar Cells. In *Organic-Inorganic Halide Perovskite Photovoltaics: From Fundamentals to Device Architectures*; Park, N.-G., Grätzel, M., Miyasaka, T., Eds.; Springer International Publishing: Cham, 2016; pp 53−77. DOI: 10.1007/978-3-319-35114-8_3.
(40) Sha, W. E. I.; Ren, X.; Chen, L.; Choy, W. C. H. The Efficiency Limit of CH3NH3PbI3 Perovskite Solar Cells. *Appl. Phys. Lett.* **2015**, *106* (22), 221104.
(41) Shockley, W.; Queisser, H. J. Detailed Balance Limit of Efficiency of P-n Junction Solar Cells. *J. Appl. Phys.* **1961**, *32* (3), 510−519.
(42) Rühle, S. Tabulated Values of the Shockley-Queisser Limit for Single Junction Solar Cells. *Sol. Energy* **2016**, *130*, 139−147.
(43) Wheeler, S.; Bryant, D.; Troughton, J.; Kirchartz, T.; Watson, T.; Nelson, J.; Durrant, J. R. Transient Optoelectronic Analysis of the Impact of Material Energetics and Recombination Kinetics on the Open-Circuit Voltage of Hybrid Perovskite Solar Cells. *J. Phys. Chem. C* **2017**, *121* (25), 13496−13506.
(44) Yang, T. C. J.; Fiala, P.; Jeangros, Q.; Ballif, C. High-Bandgap Perovskite Materials for Multijunction Solar Cells. *Joule* **2018**, *2* (8), 1421−1436.
(45) Tu, Y.; Wu, J.; Lan, Z.; He, X.; Dong, J.; Jia, J.; Guo, P.; Lin, J.; Huang, M.; Huang, Y. Modulated CH3NH3PbI3-x Brx Film for Efficient Perovskite Solar Cells Exceeding 18. *Sci. Rep.* **2017**, *7* (March), 1−8.
(46) Jesper Jacobsson, T.; Correa-Baena, J. P.; Pazoki, M.; Saliba, M.; Schenk, K.; Grätzel, M.; Hagfeldt, A. Exploration of the Compositional Space for Mixed Lead Halogen Perovskites for High Efficiency Solar Cells. *Energy Environ. Sci.* **2016**, *9* (5), 1706−1724.
(47) Jeon, N. J.; Na, H.; Jung, E. H.; Yang, T. Y.; Lee, Y. G.; Kim, G.; Shin, H. W.; Il Seok, S.; Lee, J.; Seo, J. A Fluorene-Terminated Hole-Transporting Material for Highly Efficient and Stable Perovskite Solar Cells. *Nat. Energy* **2018**, *3* (8), 682−689.
(48) Kim, G. M.; Ishii, A.; Öz, S.; Miyasaka, T. MACl-Assisted Ge Doping of Pb-Hybrid Perovskite: A Universal Route to Stabilize High Performance Perovskite Solar Cells. *Adv. Energy Mater.* **2020**, *10* (7), 1903299.
(49) Lee, S.; Kim, D. B.; Hamilton, I.; Daboczi, M.; Nam, Y. S.; Lee, B. R.; Zhao, B.; Jang, C. H.; Friend, R. H.; Kim, J. S.; Song, M. H. Control of Interface Defects for Efficient and Stable Quasi-2D

https://doi.org/10.1021/acsenergylett.1c02044
ACS Energy Lett. 2021, 6, 3970−3981

Perovskite Light-Emitting Diodes Using Nickel Oxide Hole Injection Layer. *Adv. Sci.* **2018**, *5* (11), 1801350.
(50) Lin, C. T.; Lee, J.; Kim, J. S.; Macdonald, T. J.; Ngiam, J.; Xu, B.; Daboczi, M.; Xu, W.; Pont, S.; Park, B.; Kang, H.; Kim, J. S.; Payne, D. J.; Lee, K.; Durrant, J. R.; McLachlan, M. A. Origin of Open-Circuit Voltage Enhancements in Planar Perovskite Solar Cells Induced by Addition of Bulky Organic Cations. *Adv. Funct. Mater.* **2020**, *30* (7), 1906763.
(51) Limbu, S.; Park, K. B.; Wu, J.; Cha, H.; Yun, S.; Lim, S. J.; Yan, H.; Luke, J.; Ryu, G.; Heo, C. J.; Kim, S.; Jin, Y. W.; Durrant, J. R.; Kim, J. S. Identifying the Molecular Origins of High-Performance in Organic Photodetectors Based on Highly Intermixed Bulk Heterojunction Blends. *ACS Nano* **2021**, *15* (1), 1217−1228.
(52) Labanti, C.; Sung, M. J.; Luke, J.; Kwon, S.; Kumar, R.; Hong, J.; Kim, J.; Bakulin, A. A.; Kwon, S.-K.; Kim, Y.-H.; Kim, J.-S. Selenium-Substituted Non-Fullerene Acceptors: A Route to Superior Operational Stability for Organic Bulk Heterojunction Solar Cells. *ACS Nano* **2021**, *15*, 7700.
(53) Kronik, L.; Shapira, Y. Surface Photovoltage Phenomena: Theory, Experiment, and Applications. *Surf. Sci. Rep.* **1999**, *37* (1), 1−206.
(54) Cavalcoli, D.; Cavallini, A. Surface Photovoltage Spectroscopy -Method and Applications. *Phys. Status Solidi Curr. Top. Solid State Phys.* **2010**, *7* (5), 1293−1300.
(55) Luke, J.; Corrêa, L.; Rodrigues, J.; Martins, J.; Daboczi, M.; Bagnis, D.; Kim, J. S. A Commercial Benchmark: Light-Soaking Free, Fully Scalable, Large-Area Organic Solar Cells for Low-Light Applications. *Adv. Energy Mater.* **2021**, *11*, 2003405.
(56) Daboczi, M.; Hamilton, I.; Xu, S.; Luke, J.; Limbu, S.; Lee, J.; McLachlan, M. A.; Lee, K.; Durrant, J. R.; Baikie, I. D.; Kim, J. S. Origin of Open-Circuit Voltage Losses in Perovskite Solar Cells Investigated by Surface Photovoltage Measurement. *ACS Appl. Mater. Interfaces* **2019**, *11* (50), 46808−46817.
(57) Daboczi, M.; Kim, J. S.; Lee, J.; Kang, H.; Hamilton, I.; Lin, C. T.; Dimitrov, S. D.; McLachlan, M. A.; Lee, K.; Durrant, J. R.; Kim, J. S. Towards Efficient Integrated Perovskite/Organic Bulk Heterojunction Solar Cells: Interfacial Energetic Requirement to Reduce Charge Carrier Recombination Losses. *Adv. Funct. Mater.* **2020**, *30*, 2001482.
(58) Du, T.; Xu, W.; Xu, S.; Ratnasingham, S. R.; Lin, C. T.; Kim, J.; Briscoe, J.; McLachlan, M. A.; Durrant, J. R. Light-Intensity and Thickness Dependent Efficiency of Planar Perovskite Solar Cells: Charge Recombinationversusextraction. *J. Mater. Chem. C* **2020**, *8* (36), 12648−12655.
(59) Zhou, Y.; Wang, F.; Fang, H. H.; Loi, M. A.; Xie, F. Y.; Zhao, N.; Wong, C. P. Distribution of Bromine in Mixed Iodide-Bromide Organolead Perovskites and Its Impact on Photovoltaic Performance. *J. Mater. Chem. A* **2016**, *4* (41), 16191−16197.
(60) Lin, Q.; Armin, A.; Nagiri, R. C. R.; Burn, P. L.; Meredith, P. Electro-Optics of Perovskite Solar Cells. *Nat. Photonics* **2015**, *9* (2), 106−112.
(61) Liu, Z.; Siekmann, J.; Klingebiel, B.; Rau, U.; Kirchartz, T. Interface Optimization via Fullerene Blends Enables Open-Circuit Voltages of 1.35 V in $CH_3NH_3Pb(I_{0.8}Br_{0.2})_3$ Solar Cells. *Adv. Energy Mater.* **2021**, *11*, 2003386.
(62) Tanaka, K.; Takahashi, T.; Ban, T.; Kondo, T.; Uchida, K.; Miura, N. Comparative Study on the Excitons in Lead-Halide-Based Perovskite-Type Crystals CH3NH3PbBr3 CH3NH 3PbI3. *Solid State Commun.* **2003**, *127* (9−10), 619−623.
(63) Knupfer, M. Exciton Binding Energies in Organic Semiconductors. *Appl. Phys. A: Mater. Sci. Process.* **2003**, *77* (5), 623−626.
(64) Miyata, A.; Mitioglu, A.; Plochocka, P.; Portugall, O.; Wang, J. T. W.; Stranks, S. D.; Snaith, H. J.; Nicholas, R. J. Direct Measurement of the Exciton Binding Energy and Effective Masses for Charge Carriers in Organic-Inorganic Tri-Halide Perovskites. *Nat. Phys.* **2015**, *11* (7), 582−587.
(65) Kim, H. S.; Lee, C. R.; Im, J. H.; Lee, K. B.; Moehl, T.; Marchioro, A.; Moon, S. J.; Humphry-Baker, R.; Yum, J. H.; Moser, J. E.; Grätzel, M.; Park, N. G. Lead Iodide Perovskite Sensitized All-Solid-State Submicron Thin Film Mesoscopic Solar Cell with Efficiency Exceeding 9. *Sci. Rep.* **2012**, *2* (7436), 591.
(66) Jeon, N. J.; Noh, J. H.; Kim, Y. C.; Yang, W. S.; Ryu, S.; Seok, S. Il. Solvent Engineering for High-Performance Inorganic-Organic Hybrid Perovskite Solar Cells. *Nat. Mater.* **2014**, *13* (9), 897−903.
(67) Song, Z.; Watthage, S. C.; Phillips, A. B.; Heben, M. J. Pathways toward High-Performance Perovskite Solar Cells: Review of Recent Advances in Organo-Metal Halide Perovskites for Photovoltaic Applications. *J. Photonics Energy* **2016**, *6* (2), 022001.
(68) Heo, J. H.; Song, D. H.; Im, S. H. Planar CH3NH3PbBr3 Hybrid Solar Cells with 10.4% Power Conversion Efficiency, Fabricated by Controlled Crystallization in the Spin-Coating Process. *Adv. Mater.* **2014**, *26* (48), 8179−8183.
(69) Wu, C. G.; Chiang, C. H.; Chang, S. H. A Perovskite Cell with a Record-High-Voc of 1.61 v Based on Solvent Annealed CH3NH3PbBr3/ICBA Active Layer. *Nanoscale* **2016**, *8* (7), 4077−4085.
(70) Du, T.; Xu, W.; Daboczi, M.; Kim, J.; Xu, S.; Lin, C. T.; Kang, H.; Lee, K.; Heeney, M. J.; Kim, J. S.; Durrant, J. R.; McLachlan, M. A. P-Doping of Organic Hole Transport Layers in p-i-n Perovskite Solar Cells: Correlating Open-Circuit Voltage and Photoluminescence Quenching. *J. Mater. Chem. A* **2019**, *7* (32), 18971−18979.
(71) Yang, W. S.; Park, B. W.; Jung, E. H.; Jeon, N. J.; Kim, Y. C.; Lee, D. U.; Shin, S. S.; Seo, J.; Kim, E. K.; Noh, J. H.; Seok, S. Il. Iodide Management in Formamidinium-Lead-Halide-Based Perovskite Layers for Efficient Solar Cells. *Science (Washington, DC, U. S.)* **2017**, *356* (6345), 1376−1379.
(72) Stolterfoht, M.; Wolff, C. M.; Márquez, J. A.; Zhang, S.; Hages, C. J.; Rothhardt, D.; Albrecht, S.; Burn, P. L.; Meredith, P.; Unold, T.; Neher, D. Visualization and Suppression of Interfacial Recombination for High-Efficiency Large-Area Pin Perovskite Solar Cells. *Nat. Energy* **2018**, *3* (10), 847−854.
(73) Yoon, S. J.; Kuno, M.; Kamat, P. V. Shift Happens. How Halide Ion Defects Influence Photoinduced Segregation in Mixed Halide Perovskites. *ACS Energy Lett.* **2017**, *2* (7), 1507−1514.
(74) Duong, T.; Mulmudi, H. K.; Wu, Y.; Fu, X.; Shen, H.; Peng, J.; Wu, N.; Nguyen, H. T.; Macdonald, D.; Lockrey, M.; White, T. P.; Weber, K.; Catchpole, K. Light and Electrically Induced Phase Segregation and Its Impact on the Stability of Quadruple Cation High Bandgap Perovskite Solar Cells. *ACS Appl. Mater. Interfaces* **2017**, *9* (32), 26859−26866.
(75) Brennan, M. C.; Draguta, S.; Kamat, P. V.; Kuno, M. Light-Induced Anion Phase Segregation in Mixed Halide Perovskites. *ACS Energy Lett.* **2018**, *3* (1), 204−213.
(76) Aristidou, N.; Eames, C.; Sanchez-Molina, I.; Bu, X.; Kosco, J.; Saiful Islam, M.; Haque, S. A. Fast Oxygen Diffusion and Iodide Defects Mediate Oxygen-Induced Degradation of Perovskite Solar Cells. *Nat. Commun.* **2017**, *8*, 15218.
(77) Jacobsson, T. J.; Schwan, L. J.; Ottosson, M.; Hagfeldt, A.; Edvinsson, T. Determination of Thermal Expansion Coefficients and Locating the Temperature-Induced Phase Transition in Methylammonium Lead Perovskites Using X-Ray Diffraction. *Inorg. Chem.* **2015**, *54* (22), 10678−10685.
(78) Kong, W.; Ye, Z.; Qi, Z.; Zhang, B.; Wang, M.; Rahimi-Iman, A.; Wu, H. Characterization of an Abnormal Photoluminescence Behavior upon Crystal-Phase Transition of Perovskite CH3NH3PbI3. *Phys. Chem. Chem. Phys.* **2015**, *17* (25), 16405−16411.
(79) Liu, Y.; Lu, H.; Niu, J.; Zhang, H.; Lou, S.; Gao, C.; Zhan, Y.; Zhang, X.; Jin, Q.; Zheng, L. Temperature-Dependent Photoluminescence Spectra and Decay Dynamics of MAPbBr3 and MAPbI3 Thin Films. *AIP Adv.* **2018**, *8* (9), 095108.
(80) Boopathi, K. M.; Martín-García, B.; Ray, A.; Pina, J. M.; Marras, S.; Saidaminov, M. I.; Bonaccorso, F.; Di Stasio, F.; Sargent, E. H.; Manna, L.; Abdelhady, A. L. Permanent Lattice Compression of Lead-Halide Perovskite for Persistently Enhanced Optoelectronic Properties. *ACS Energy Lett.* **2020**, *5* (2), 642−649.
(81) Liu, G.; Kong, L.; Gong, J.; Yang, W.; Mao, H. K.; Hu, Q.; Liu, Z.; Schaller, R. D.; Zhang, D.; Xu, T. Pressure-Induced Bandgap Optimization in Lead-Based Perovskites with Prolonged Carrier

https://doi.org/10.1021/acsenergylett.1c02044
ACS Energy Lett. 2021, 6, 3970−3981

Lifetime and Ambient Retainability. *Adv. Funct. Mater.* **2017**, *27* (3), 1604208.
(82) Yuan, Y.; Huang, J. Ion Migration in Organometal Trihalide Perovskite and Its Impact on Photovoltaic Efficiency and Stability. *Acc. Chem. Res.* **2016**, *49* (2), 286−293.
(83) Meloni, S.; Moehl, T.; Tress, W.; Franckeviius, M.; Saliba, M.; Lee, Y. H.; Gao, P.; Nazeeruddin, M. K.; Zakeeruddin, S. M.; Rothlisberger, U.; Graetzel, M. Ionic Polarization-Induced Current-Voltage Hysteresis in $CH_3NH_3PbX_3$ perovskite Solar Cells. *Nat. Commun.* **2016**, *7*, 10334.
(84) Xu, J.; Boyd, C. C.; Yu, Z. J.; Palmstrom, A. F.; Witter, D. J.; Larson, B. W.; France, R. M.; Werner, J.; Harvey, S. P.; Wolf, E. J.; Weigand, W.; Manzoor, S.; Van Hest, M. F. A. M.; Berry, J. J.; Luther, J. M.; Holman, Z. C.; McGehee, M. D. Triple-Halide Wide-Band Gap Perovskites with Suppressed Phase Segregation for Efficient Tandems. *Science (Washington, DC, U. S.)* **2020**, *367* (6482), 1097−1104.
(85) Zisman, W. A. A. New Method of Measuring Contact Potential Differences in Metals. *Rev. Sci. Instrum.* **1932**, *3* (7), 367−370.
(86) Baikie, I. D.; Estrup, P. J. Low Cost PC Based Scanning Kelvin Probe. *Rev. Sci. Instrum.* **1998**, *69* (11), 3902−3907.
(87) Shimizu, H.; Munakata, C. Nondestructive Diagnostic Method Using Ac Surface Photovoltage for Detecting Metallic Contaminants in Silicon Wafers. *J. Appl. Phys.* **1993**, *73* (12), 8336−8339.
(88) Schroder, D. K. Surface Voltage and Surface Photovoltage: History, Theory and Applications. *Meas. Sci. Technol.* **2001**, *12* (3), R16−R31.
(89) Nakhmanson, R. S. Frequency Dependence of the Photo-EMF of Strongly Inverted Ge and Si MIS Structures-I. Theory. *Solid-State Electron.* **1975**, *18*, 617−626.
(90) Nakhmanson, R. S.; Ovsyuk, Z. S.; Popov, L. K. Frequency Dependence of the Photo-EMF of Strongly Inverted Ge and Si MIS Structures-II Experiments. *Solid-State Electron.* **1975**, *18*, 627−634.
(91) Zhang, W.; Pathak, S.; Sakai, N.; Stergiopoulos, T.; Nayak, P. K.; Noel, N. K.; Haghighirad, A. A.; Burlakov, V. M.; Dequilettes, D. W.; Sadhanala, A.; Li, W.; Wang, L.; Ginger, D. S.; Friend, R. H.; Snaith, H. J. Enhanced Optoelectronic Quality of Perovskite Thin Films with Hypophosphorous Acid for Planar Heterojunction Solar Cells. *Nat. Commun.* **2015**, *6* (May), 10030.
(92) Bergmann, V. W.; Guo, Y.; Tanaka, H.; Hermes, I. M.; Li, D.; Klasen, A.; Bretschneider, S. A.; Nakamura, E.; Berger, R.; Weber, S. A. L. Local Time-Dependent Charging in a Perovskite Solar Cell. *ACS Appl. Mater. Interfaces* **2016**, *8* (30), 19402−19409.
(93) Leijtens, T.; Eperon, G. E.; Barker, A. J.; Grancini, G.; Zhang, W.; Ball, J. M.; Kandada, A. R. S.; Snaith, H. J.; Petrozza, A. Carrier Trapping and Recombination: The Role of Defect Physics in Enhancing the Open Circuit Voltage of Metal Halide Perovskite Solar Cells. *Energy Environ. Sci.* **2016**, *9* (11), 3472−3481.
(94) Pockett, A.; Eperon, G. E.; Sakai, N.; Snaith, H. J.; Peter, L. M.; Cameron, P. J. Microseconds, Milliseconds and Seconds: Deconvoluting the Dynamic Behaviour of Planar Perovskite Solar Cells. *Phys. Chem. Chem. Phys.* **2017**, *19* (8), 5959−5970.

https://doi.org/10.1021/acsenergylett.1c02044
ACS Energy Lett. 2021, 6, 3970−3981